J. Fluid Mech. (1996), vol. 309, pp. 183–209

The behaviour of a gas cavity impacted by a weak or strong shock wave

By ZHONG DING AND S. M. GRACEWSKI
Department of Mechanical Engineering, University of Rochester, Rochester, NY 14627, USA

(Received 1 June 1995 and in revised form 12 October 1995)

Two-dimensional simulations of gas cavity responses to both weak shocks ($p \leqslant 30$ MPa) and strong shocks (p ranging from 500 to 2000 MPa) are performed using a finite volume method. An artificial viscosity to capture the shock and a simple, stable, and adaptive mesh generation technique have been developed for the computations. The details of the shock propagation, rarefaction, transmission and bubble wall motions are obtained from the numerical computations. A weak shock is defined in the present context as one that does not cause liquid jet formation upon impact with the bubble. For this case, a large pressure is created within the gas upon collapse due to rapid compression of the gas, ultimately causing the re-expansion of the bubble. The bubble collapse and re-expansion time predicted by this model agree well with spherically symmetric computations. When impacted by strong shock waves, the bubble will collapse and a liquid jet is formed that propagates through the bubble to the opposite bubble wall. Jet speeds as high as 2000 m s^{-1} are predicted by this model.

1. Introduction

An understanding of the response of a gas cavity in a fluid to a time-dependent pressure wave is important in a wide range of situations including (1) cavitation damage to human tissues during diagnostic ultrasound or lithotripsy (Delius *et al.* 1987, 1988; Bailey *et al.* 1994; and Carstensen *et al.* 1990); (2) fragmentation of gallstones or kidney stones by shock waves (Sass *et al.* 1991, Vakil & Everbach 1991; Gracewski *et al.* 1993 and Crum 1988); (3) production of 'hot spots' that cause ignition (Madar 1965); and (4) solid erosion (Kornfeld & Suvorov 1944; and Hansson & Morch 1980). The cavities may collapse nearly symmetrically, causing very high pressures within the gas. On the other hand, if the collapse becomes non-symmetric, liquid jets can be produced that can lead to pitting and erosion of nearby solid surfaces.

1.1. *Analysis of spherical bubble collapse*

The classical analysis of Rayleigh (1917) considers the collapse of an isolated, empty spherical cavity of initial radius r_0, in a liquid with density ρ, under an instantaneously applied constant hydrostatic pressure $p_0(t) = p_\infty H\langle t\rangle$, where $H\langle t\rangle$ is the unit step function. Assuming incompressible and inviscid behaviour of the liquid, Rayleigh's analysis gives the time for the cavity to collapse as $t \approx 0.91468 r_0(\rho/p_\infty)^{1/2}$, which is reasonably accurate. However the predicted collapse pressure tends to infinity as the cavity radius approaches zero. In practice, a cavity cannot be considered as empty, and thermal effects and liquid compressibility should be considered.

After Rayleigh, many researchers investigated the behaviour of a gas cavity in

response to applied pressure fields, and many models for bubble dynamics were proposed that assume spherically symmetric collapse of the bubble. Among them, Flynn (1964) and Plesset & Prosperetti (1977) take into account the gas within the bubble, but neglect the liquid compressibility, Trilling (1952) assumes small compression of the liquid, and Gilmore (1952) accounts for the fluid compressibility. Each of these formulations accounts for the gas pressure, surface tension and the liquid viscosity, and therefore is more realistic than the Rayleigh formulation. The inclusion of an elastic membrane in the Gilmore equation was proposed by Ding & Gracewski (1994) to investigate the effects of a confining membrane on bubble behaviour in response to applied pressures fields. Each of these formulations is investigated numerically since it is difficult to find the analytical solutions for these nonlinear equations.

1.2. *Experimental investigation*

Kornfeld & Suvorov (1944) were the first to suggest that cavities might collapse asymmetrically and produce a jet. Later on, many experiments and analyses proved the existence of a jet in a cavity collapsing asymmetrically. Such asymmetric bubble collapse can occur when a bubble is near a solid or gas interface or when a bubble is impacted by a strong shock wave.

Since the 1960s, a number of researchers have studied the behaviour of bubbles near interfaces. For example, Vogel, Lauterborn & Timm (1989) studied laser-produced cavitation bubbles near a solid boundary. By using high-speed photography with up to 1 million frames per second, they observed jet and counter-jet formation, and the development of a ring vortex resulting from the jet flow near the solid boundary.

More recently, bubble response to incident shock waves has also been studied experimentally. Dear & Field (1987) made cylindrical cavities in a gel to observe the collapse in these cavities when they are impinged by a shock. A striker was projected to impact the gel, and high-speed photography was used to record the behaviour of the cavities and jet formation under such impact. For an impact pressure of 0.26 GPa, a 3 mm bubble will generate a jet with a velocity of about 400 m s^{-1}.

Bourne & Field (1990) reported the results of a high-speed photographic study of cavities collapsed asymmetrically by shocks of strengths in the range of 0.26 to 3.5 GPa. The collapse of a 3 mm cavity in gelatine under a shock of strength 0.26 GPa will have a velocity of 300 m s^{-1}. Under a shock of strength 1.88 GPa, the jet velocity is up to 5000 m s^{-1} for a 6 mm bubble.

Philipp *et al.* (1993) also used high-speed photography and observed jet formation in a gas cavity induced by lithotripter-generated shock waves. They used peak shock source pressures of 65 and 102 MPa, and reported a peak jet speed of up to 770 m s^{-1} at the moment of collapse. The collapse time measured in these experiments ranges from 1 μs to 9 μs for bubbles with an initial radius between 0.15 and 1.2 mm.

A liquid jet striking a solid surface will generate an impact pressure with a magnitude that can be estimated using the 'water hammer' equation as

$$p = \rho_L c_L u \left(\frac{\rho_S c_S}{\rho_L c_L + \rho_S c_S} \right), \tag{1.1}$$

where ρ, c, u are density, sound speed and particle velocity, respectively, and subscript S refers to solid and subscript L refers to liquid. Usually, $\rho_S c_S \gg \rho_L c_L$, so $p \approx \rho_L c_L u$. The 'water hammer' equation can be used along with the experimentally measured velocity to estimate the damage the bubble collapse might cause on nearby solids. However, to the authors' knowledge, no model yet exists to predict the bubble response to a range of shock wave fields or to describe the detailed pressure and velocity fields

that are generated. This information is important for a better understanding of cavitation phenomena and the possible cavitation damage to solids subjected to shock waves.

1.3. *Analysis of axisymmetric bubble collapse*

In most numerical models used for the analysis of bubble collapse near planar interfaces, the liquid surrounding the bubble is assumed to be inviscid, incompressible, and irrotational. (See review articles by Steinberg 1993, Blake & Gibson 1987, and Prosperetti 1982.) The first fully numerical model for collapse of a bubble near a rigid boundary was presented by Plesset & Prosperetti (1977). They integrated Bernoulli's equation numerically and demonstrated the asymmetric collapse of a gas cavity near the boundary due to asymmetry of the resulting pressure field. Blake & Gibson (1987) used a boundary integral method to compute the growth and collapse of transient vapour cavities near a rigid boundary when subject to an incident stagnation-point flow in the presence of buoyancy forces. They found that the direction of the liquid jet can be either toward or away from the boundary depending on the flow parameters. Sato, Tomita & Shima (1994) also used a boundary integral method to simulate bubble behaviour for gas bubbles near a rigid boundary subjected to an oscillatory pressure field. In addition, they applied the method of images to solve the differential equations describing the nonlinear oscillation and migration of the bubble. In these three models, computation had to be stopped when the liquid jet reached the opposite bubble boundary.

Recently, techniques have been developed, assuming a ring-bubble geometry, that allow further computation as the liquid jet penetrates the opposite boundary. Using a boundary element method with conventional and hypersingular equations, Zhang, Duncan & Chahine (1993) investigated the final stages of bubble collapse near a rigid wall. They were able to calculate the pressure generated by the jet impacting the rigid boundary.

Tipton, Steinberg & Tomita (1992) considered the effect of fluid compressibility on bubble collapse near a rigid boundary. They used an ALE (Arbitrary Lagrangian Eulerian) hydrodynamics code to obtain pressure fields and bubble response. They were able to continue calculations even after the jet impacted the opposite bubble wall and therefore were able to obtain a prediction for pressures generated along the rigid interface.

Numerical studies of shock wave interactions with bubbles have mainly been limited to gas bubbles within a gas medium (Quirk & Karni 1994; Evans, Harlow & Meixner 1962; Haas & Sturtevant 1987; Schwendeman 1986; and Picone & Boris 1988). Grove & Menikoff (1990) presented results for weak and strong shock waves interacting with a gas bubble in water. Their main interest is in the anomalous reflection and diffraction of shock waves at interfaces and therefore their results are limited to times during which the shock wave is interacting with the bubble.

1.4. *Scope of the paper*

In this paper, the Euler equations in cylindrical coordinates with axisymmetry are used to investigate a gas cavity response to a step shock wave. To accurately model the shock wave propagation, compressibility of the fluid must be taken into account. Both weak and strong shocks are used in the numerical simulations. The reflection, transmission, and refraction of the shock waves as well as the velocity fields near the gas cavity are investigated to provide a clear view of the bubble responses under various shock conditions. The responses of a gas cavity to weak shocks

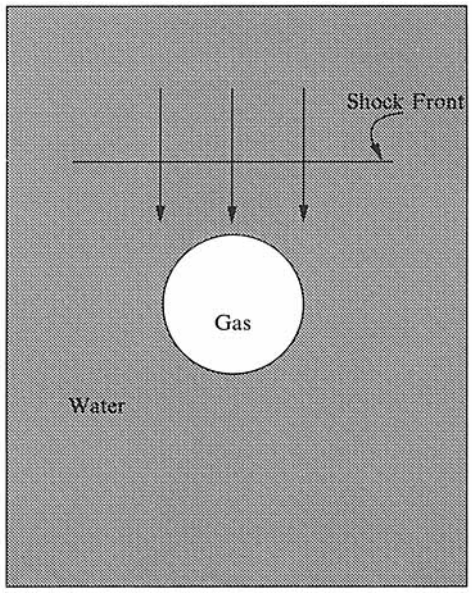

FIGURE 1. The problem geometry.

are compared to results predicted by the one-dimensional Gilmore model to help identify the conditions under which the spherically–symmetric model can be used to predict the response of a gas cavity to shock waves. In addition, responses to strong shock waves and the resulting jet formation and velocity fields are presented and discussed.

2. Two-dimensional simulation of a spherical gas cavity

The problem considered consists of an initially spherical gas cavity in statical equilibrium with the surrounding liquid that is struck by a planar shock wave propagating in the liquid as shown in figure 1. To generate a model to simulate the gas cavity response to shock waves, the following assumptions are made:

(i) The problem is axisymmetric.
(ii) It is an adiabatical process except within the shock front.
(iii) The body force, surface tension and shear viscosity are negligible.
(iv) Diffusion across the water–gas interface is neglected.

The conservation equations (2.1*a–d*) in a cylindrical coordinate system, as well as the water equation of state as describe by Steinberg (1987) and the ideal gas equation of state govern the response of the two fluids. In the computation program, derivatives in time are evaluated along the motion of the fluid. They are Lagrangian and denoted by d/dt. A more detailed discussion of the discretization techniques can be found in SHALE (Demuth *et al.* 1985). The conservation equations are

$$\frac{\partial \rho}{\partial t} + \frac{\partial \rho u_r}{\partial r} + \frac{\partial \rho u_z}{\partial z} + \frac{\rho u_r}{r} = 0, \tag{2.1a}$$

$$\rho \frac{\mathrm{d}u_r}{\mathrm{d}t} = -\frac{\partial p}{\partial r} + \frac{\partial \Sigma_{rr}}{\partial r} + \frac{\partial \Sigma_{rz}}{\partial z} + \frac{\Sigma_{rr} - \Sigma_{\theta\theta}}{r}, \tag{2.1b}$$

$$\rho\frac{\mathrm{d}u_z}{\mathrm{d}t} = -\frac{\partial p}{\partial z} + \frac{\partial \Sigma_{zz}}{\partial z} + \frac{\partial \Sigma_{zr}}{\partial r} + \frac{\Sigma_{zr}}{r}, \tag{2.1c}$$

$$\rho\frac{\mathrm{d}e}{\mathrm{d}t} = -p\nabla\cdot\boldsymbol{u} + \Sigma_{rr}\varepsilon_{rr} + \Sigma_{zz}\varepsilon_{zz} + \Sigma_{\theta\theta}\varepsilon_{\theta\theta} + \Sigma_{rz}\varepsilon_{rz}, \tag{2.1d}$$

where ρ is the specific density, t is the time, r and z are the axisymmetric coordinates, u_r and u_z are the velocity components, e is the specific internal energy, p is the hydrostatic pressure, ε is the shearing rate tensor, and Σ is the artificial viscosity tensor which will be discussed later.

2.1. *The numerical scheme*

We developed a computation program to solve the axisymmetric Euler equations based on the finite volume methods of Wilkins (1964). We also borrowed many computation techniques from the hydrodynamics codes SALE (Hirt, Amsden & Cook 1974) and SHALE (Demuth *et al.* 1985), which are arbitrary Lagrangian and Eulerian codes combining the advantages of both the Lagrangian and Eulerian methods.

To capture the shock, we designed an artificial viscosity based on previous works and the physics of the shock. We also designed a weighting method in mesh generation that will generate finer meshes near the shock front and around the gas cavity where the pressure gradients are much higher than in other regions in the computational domain.

2.2. *The artificial viscosities*

The Navier–Stokes equations admit discontinuous solutions, including shocks and contact discontinuities. If no artificial viscosity is added in the numerical computation, large oscillations in density, velocity, etc. will occur behind the shock front since the numerical equations do not predict enough conversion of kinetic energy to internal energy.

The artificial viscosity methods introduce a dissipative term in the shock front, to allow the discontinuous shock propagation to be approximated by a continuous description. Neumann & Richtmyer (1950) were the first to propose a method of capturing shocks in one-dimensional hydrocodes by introducing an artificial viscosity q in the form

$$q = -\frac{(c_q\Delta x)^2}{V}\frac{\partial u}{\partial x}\left|\frac{\partial u}{\partial x}\right|, \tag{2.2}$$

where Δx is the mesh size, u is the particle velocity, V is the volume, and c_q is a constant near unity.

Landshoff (1955) added a linear term in the Von Neumann-type artificial viscosity, and obtained another artificial viscosity for one-dimensional hydrocodes, in the form

$$q = c_q\rho(\Delta u)^2 + c_l c_s\rho|\Delta u|, \tag{2.3}$$

where Δu is the difference in particle velocity across the mesh, c_q and c_l are constants of the order of unity, and c_s is the local sound speed. The linear term in the artificial viscosity is effective in damping out the non-physical oscillations after the shock propagates through the medium. For this reason, it does a better job than the Von Neumann artificial viscosity.

In two dimensions, Wilkins (1980) designed an artificial viscosity accounting for the non-regular mesh size by defining an equivalent cell length in the direction of the acceleration. The equivalent cell length L is defined as the cell area divided by the

calculated average thickness of the zone normal to the direction of acceleration. The artificial viscosity q is given as

$$q = c_q^2 \rho L^2 \left(\frac{\mathrm{d}s}{\mathrm{d}t}\right)^2 + c_l \rho L c_s \left|\frac{\mathrm{d}s}{\mathrm{d}t}\right|, \tag{2.4}$$

where $q = 0$ for $\mathrm{d}s/\mathrm{d}t \geqslant 0$, c_s is the sound speed, $c_q \approx 2$, $c_L \approx 1$, and

$$L = \frac{2A}{d_1 + d_2 + d_3 + d_4}, \tag{2.5}$$

$$\frac{\mathrm{d}s}{\mathrm{d}t} = \frac{\partial \dot{x}}{\partial x}\cos^2\alpha + \frac{\partial \dot{y}}{\partial y}\sin^2\alpha + \left(\frac{\partial \dot{x}}{\partial y} + \frac{\partial \dot{y}}{\partial x}\right)\cos\alpha \sin\alpha. \tag{2.6}$$

Here A is the area of the cell, and d_i is the perpendicular distance from node i to a line through the cell centre in the direction of acceleration, and α is angle between this line and the x-axis. This artificial viscosity does not perform well in meshes with large aspect ratios.

Margolin (1988) designed an artificial viscosity based on the assumption that the resultant forces of the artificial viscosity should be in the direction of the relative velocity, $\Delta \boldsymbol{u}$, rather than along the edge of a cell. He assumed no hourglass in the cell, i.e.

$$\boldsymbol{u}_1 - \boldsymbol{u}_2 + \boldsymbol{u}_3 - \boldsymbol{u}_4 = 0, \tag{2.7}$$

where $\boldsymbol{u}_i$ is the velocity of node i. The velocity difference of a cell's nodes is computed in terms of the spatial gradients of the velocity in the cell, not the difference of actual velocities of the nodes. He defined two vectors using the four node points of a mesh:

$$\boldsymbol{k} = 0.5(x_2 + x_3 - x_1 - x_4, y_2 + y_3 - y_1 - y_4),$$
$$\boldsymbol{l} = 0.5(x_3 + x_4 - x_1 - x_2, y_3 + y_4 - y_1 - y_2).$$

For the cell-centred artificial viscosity to produce inter-nodal forces in the velocity difference direction, he constructed the artificial viscosity

$$q_{\alpha\beta} = \rho W \frac{\partial u_\alpha}{\partial x_\gamma}[k_\gamma k_\beta + l_\gamma l_\beta], \tag{2.8}$$

where

$$W = \max\left[\frac{c_l c_s + c_q\left|\frac{\partial u_\alpha}{\partial x_\gamma}k_\gamma\right|}{|\boldsymbol{k}|}, \frac{c_l c_s + c_q\left|\frac{\partial u_\alpha}{\partial x_\gamma}l_\gamma\right|}{|\boldsymbol{l}|}\right], \tag{2.9}$$

and $c_l \approx 1$, $c_q \approx 1$, and c_s is sound speed. The four components of the tensor artificial viscosity are used as the real stress components in accelerating the nodes and in computing the energy. The artificial viscosity is turned on only when the cell is compressed.

Benson (1991) designed a flux-limiting artificial viscosity by using a monotonicity limiting technique (Leer 1977, 1979) in computing the velocity jump and defining the cell principal strain direction as the shock direction. Benson's artificial viscosity performed better than those discussed above as reported in his paper.

Since the velocity change across a shock is normal to the shock front (Thompson 1988), we defined the shock propagation direction in terms of the velocity differences of the nodes on each side of a cell. This velocity difference is computed using the

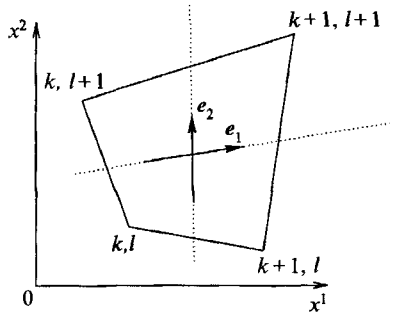

FIGURE 2. The two base vectors e_1 and e_2 in the mesh coordinate system.

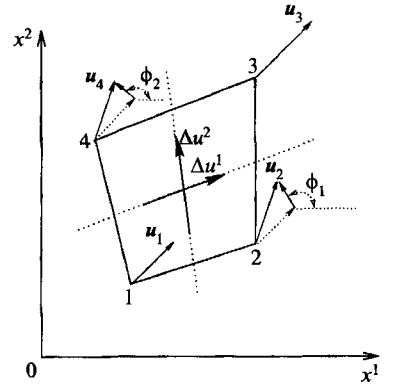

FIGURE 3. Velocity jump in the mesh coordinate system and the direction of nodal velocity differences for the two velocity jumps.

velocity gradients of the cell. The velocity jump across a mesh is computed in the same way as in Benson's artificial viscosity (Benson 1991). This jump is first computed in the mesh coordinate system, is then transferred to the Cartesian coordinate system, and is finally projected to the shock propagation direction. In the shock direction, an artificial viscosity is constructed which includes the linear and quadratic terms. A coordinate transformation is performed so as to obtain the artificial viscosity in the Cartesian coordinates. The artificial viscosity is turned on only when the cell is compressed, i.e. $\nabla \cdot \boldsymbol{u} < 0$. The detailed design of this artificial viscosity is given below.

As in Benson's method (Benson 1991), $\boldsymbol{e}_i = X_i^j \boldsymbol{E}_j$ are defined as the base vectors in the mesh coordinate system (figure 2), where $\boldsymbol{E}_j$ are the the unit vectors in the Cartesian coordinate system (x^1, x^2), and

$$X_i^1 = \tfrac{1}{2}[x^i(k+1,l) - x^i(k,l) + x^i(k+1,l+1) - x^i(k,l+1)], \tag{2.10}$$

$$X_i^2 = \tfrac{1}{2}[x^i(k,l+1) - x^i(k,l) + x^i(k+1,l+1) - x^i(k+1,l)]. \tag{2.11}$$

The two velocity jumps Δu^1 and Δu^2 are computed in the same way as in Benson's artificial viscosity (Benson 1991). In figure 3, Δu^1 is the velocity jump across side $1-4$ and $2-3$, and Δu^2 is the velocity jump across side $1-2$ and $3-4$. Therefore the direction for Δu^1 is determined by the velocity difference between node 1 and node 4, which is $\Delta \boldsymbol{u}_{41} = \boldsymbol{u}_4 - \boldsymbol{u}_1$. A unit vector $\boldsymbol{a}_1$ (equation (2.12)) is defined in the direction of $\Delta \boldsymbol{u}_{41}$. Similarly, a unit vector $\boldsymbol{a}_2$ (equation (2.13)) is defined as the direction for the velocity jump Δu^2, and is determined by the velocity difference between node 1 and

node 2.† The two unit vectors $\boldsymbol{a}_1$ and $\boldsymbol{a}_2$ are computed as

$$\boldsymbol{a}_1 = \cos(\phi_1)\boldsymbol{E}_1 + \sin(\phi_1)\boldsymbol{E}_2, \tag{2.12}$$

$$\boldsymbol{a}_2 = \cos(\phi_2)\boldsymbol{E}_1 + \sin(\phi_2)\boldsymbol{E}_2, \tag{2.13}$$

where

$$\phi_1 = \tan^{-1}\left(\frac{(\partial u_2/\partial x_\beta)X_1^\beta}{(\partial u_1/\partial x_\beta)X_1^\beta}\right), \tag{2.14}$$

$$\phi_2 = \tan^{-1}\left(\frac{(\partial u_2/\partial x_\beta)X_2^\beta}{(\partial u_1)/(\partial x_\beta)X_2^\beta}\right) \tag{2.15}$$

The velocity jumps Δu^1 and Δu^2 are transferred to the Cartesian coordinate system

$$\Delta \boldsymbol{u}^1 = \Delta u^1 X_1^1 \boldsymbol{E}_1 + \Delta u^1 X_1^2 \boldsymbol{E}_2, \tag{2.16}$$

$$\Delta \boldsymbol{u}^2 = \Delta u^2 X_2^1 \boldsymbol{E}_1 + \Delta u^2 X_2^2 \boldsymbol{E}_2. \tag{2.17}$$

The velocity differences in the shock propagation direction can be computed as

$$\Delta u_s^1 = \boldsymbol{a}_1 \cdot \Delta \boldsymbol{u}^1 = \Delta u^1 X_1^1 \cos(\phi_1) + \Delta u^1 X_1^2 \sin(\phi_1),$$
$$\Delta u_s^2 = \boldsymbol{a}_2 \cdot \Delta \boldsymbol{u}^2 = \Delta u^2 X_2^1 \cos(\phi_2) + \Delta u^2 X_2^2 \sin(\phi_2).$$

The artificial viscosity is then constructed in the two velocity difference directions

$$Q_1^{11} = -\rho[c_l c_s|\Delta u_s^1| + c_q(\Delta u_s^1)^2], \tag{2.18}$$

$$Q_2^{11} = -\rho[c_l c_s|\Delta u_s^2| + c_q(\Delta u_s^2)^2], \tag{2.19}$$

where ρ is the density, c_l and c_q are constants typically in the range 0.3–1.5, and c_s is the local sound speed. The above artificial viscosities are transferred back to the Cartesian coordinate system:

$$\Sigma_{ij} = Q_1^{11} l_{i1}^1 l_{j1}^1 + Q_2^{11} l_{i1}^2 l_{j1}^2, \tag{2.20}$$

where

$$l_{11}^1 = \cos(\phi_1), \quad l_{21}^1 = -\sin(\phi_1), \quad l_{11}^2 = \cos(\phi_2), \quad l_{21}^2 = -\sin(\phi_2).$$

2.3. *Mesh generation*

In a discretized computation, the meshing techniques are important in obtaining an accurate approximation for the continuous system as well as in determining the efficiency of the program. A smooth and rectangular mesh is desirable. When a large deformation is involved, a technique is needed to regenerate the mesh so that it will remain smooth and regular. In many problems, the gradient of some parameters can be much higher in some regions than that in other regions of the computational domain. It is desirable that the mesh be finer in the region of higher gradients since the rate of change is usually higher at these locations. When a shock is involved, it is desirable to have a finer mesh near the shock front so that the shock front will be defined by a thin layer in the computational mesh.

2.3.1. *Adaptive zoning*

A very simple, efficient and widely used mesh generation technique is the 'equal-potential method' designed by Winslow (1963), which generates a uniform mesh in the

† Under the assumption of no hourglass, equation (2.7) shows that $\Delta \boldsymbol{u}_{41} = \Delta \boldsymbol{u}_{32}$ and $\Delta \boldsymbol{u}_{21} = \Delta \boldsymbol{u}_{34}$.

computation domain. This technique was used in generating the initial computation mesh. Brackbill & Saltzman (1982) designed another mesh generation method, which extended Winslow's methods to adaptively vary the zone sizes and orthogonality of the grid lines in the resulting mesh. Many other investigators also developed methods of generating the adaptive mesh (Matsuno & Dwyer 1988; Dwyer, Kee & Sanders 1980; Jordan & Spaulding 1993; Thompson, Warsi & Mastin 1985). In our program, we designed a stable and efficient weighting method by adapting the mesh size with the pressure gradient and combined the adaptive methods proposed by Brackbill & Saltzman in the re-zoning process of computations.

Brackbill & Saltzman (1982) observed that the differential properties of the mapping determine the properties of the computation mesh. The global smoothness of the mapping on domain D is measured by the integral

$$I_s = \int_D [(\nabla\xi)^2 + (\nabla\eta)^2]\mathrm{d}V. \tag{2.21}$$

The orthogonality of the mapping is measured by

$$I_o = \int_D (\nabla\xi \cdot \nabla\eta)^2 J^3 \mathrm{d}V, \tag{2.22}$$

and the weighted volume variation is measured by

$$I_V = \int_D wJ\mathrm{d}V, \tag{2.23}$$

where ξ and η are the mesh coordinates, J is the Jacobian, and $w(x, y)$ is a given weight function. The smoothest mapping can be obtained by minimizing I_s, the most orthogonal mapping by minimizing I_o, and the mapping with specified variation of J by minimizing I_V.

To formulate minimization problems with unique solutions, the minimization of I_o or I_V is combined with I_s. That is, the integral I is minimized, where

$$I = I_s + \lambda_V I_V + \lambda_o I_o, \tag{2.24}$$

with $\lambda_V \geqslant 0$, and $\lambda_o \geqslant 0$.

An approximate solution to the minimization problem, which represents the desired mesh, is obtained by Gauss–Seidel iteration. In generating an initial computational mesh, 100 iterations are typically performed. For re-zone computation, three iterations are enough to generate the required mesh.

2.3.2. *The weight function*

In our program, the weight function for the mesh generation is the pressure gradient. The pressure gradient is an indicator of rate of change of parameters, such as velocity, density and momentum. Therefore, at the location where the pressure gradient is high, the rate of the change of parameters is high as well and finer meshes are needed. To obtain the pressure gradient in the computation meshes, the following formula is used:

$$w_{ij} = \left(\frac{1}{p}\frac{\partial p}{\partial x}\right)^2_{ij} + \left(\frac{1}{p}\frac{\partial p}{\partial y}\right)^2_{ij}. \tag{2.25}$$

The finite difference method in Brackbill & Saltzman (1982) is used to obtain the weight function in the finite difference form.

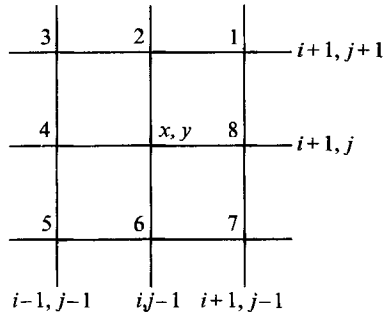

FIGURE 4. The meshes showing the numbering system.

2.3.3. *Application of weight function*

The original weighted volume variation method in equation (2.23) is cumbersome to implement in the numerical program and is not always convergent in the iteration process. Therefore, we designed another method of applying the weighted function that is efficient, stable and easy to implement in the program, and is described below.

In one dimension, or along a straight boundary, we can always locate the new position of a grid point using the average of the surrounding two grids to obtain a smooth grid distribution:

$$x_i^s = \tfrac{1}{2}(x_{i-1} + x_{i+1}). \tag{2.26}$$

If we need a mesh to be weighted by the weight function, we can use the formulation

$$x_i^w = \bar{w}_{i-1}x_{i-1} + \bar{w}_{i+1}x_{i+1}, \tag{2.27}$$

where the weight functions $\bar{w}_i$ are normalized, i.e. $\bar{w}_{i-1} + \bar{w}_{i+1} = 1$, with $\bar{w}_{i-1} = w_{i-1}/(w_{i-1} + w_{i+1})$, and $\bar{w}_{i+1} = w_{i+1}/(w_{i-1} + w_{i+1})$. We combine both smooth and weight methods by the formula

$$x_i = \frac{\lambda_s x_i^s + x_i^w}{\lambda_s + 1}. \tag{2.28}$$

The constant λ_s in equation (2.28) provides the means of controlling smoothness and weighting and is determined by numerical experiments. In the computational program, λ_s is typically in the range 2–4.

In two dimensions, we use the surrounding four grid points as the weighting points for a grid point. In figure 4, points 2, 4, 6, and 8 are used as weighting points for x_{ij}. The weight functions are normalized, i.e. $\bar{w}_2 + \bar{w}_4 + \bar{w}_6 + \bar{w}_8 = 1$. The generated grid points are

$$\boldsymbol{x}_{ij}^w = \bar{w}_2\boldsymbol{x}_2 + \bar{w}_4\boldsymbol{x}_4 + \bar{w}_6\boldsymbol{x}_6 + \bar{w}_8\boldsymbol{x}_8. \tag{2.29}$$

The Saltzman method is modified, and only the techniques to generate a mesh with control of smoothness and orthogonality are used. The positions generated by this modified Saltzman technique are written as $\boldsymbol{x}_{ij}^{so}$. We then combined our weight function techniques with the modified Saltzman method to obtain the new position of the node

$$\boldsymbol{x}_{ij} = \frac{\lambda_{so}\boldsymbol{x}_{ij}^{so} + \boldsymbol{x}_{ij}^w}{\lambda_{so} + 1}, \tag{2.30}$$

with λ_{so} as the control parameter of smoothness, orthogonality and weighting. Again, λ_{so} is determined by numerical experiments, and typically, λ_{so} is in the range 4–8 in the computations.

3. Gas cavity response to shocks

In this section, we present the computed results for the response of a gas cavity to step shock waves using the numerical techniques described in the previous section. The initial pressure is $p_0 = 0.1$ MPa. The initial radii of the gas cavities are 0.01, 0.1, and 1 cm. Both weak shocks (typically p/p_0 is in the range of 200 to 300) and strong shocks (p/p_0 ranges from 5000 to 20000) are applied. A weak shock, as defined in Thompson (1988), satisfies the relation $(p - p_0)/\rho_0 c_0^2 \ll 1$, where p is the pressure behind the shock front. And a strong shock is defined as satisfying the relation $(p - p_0)/\rho_0 c_0^2 \gg 1$. However, in this paper a weak shock is defined as a shock with a strength which will not cause a jet formation upon bubble collapse. And a strong shock is defined as a shock with a strength which will lead to a jet formation upon impact with the gas cavity.

3.1. *Response to weak shock waves*

With a shock strength of $p/p_0 = 205$, the compression of the water is very small, $\rho/\rho_0 - 1 = 0.009$. Therefore the shock wave propagation is very close to the acoustic limit. The initial density of water is 1000 kg m^{-3}, and the acoustic wave speed is 1480 m s^{-1}. For this shock strength, the shock speed is 1514 m s^{-1}, and the particle speed behind the shock front is 13.5 m s^{-1}. The initial density and acoustic wave speed in the gas are 1.2 kg m^{-3} and 343 m s^{-1}, respectively, with ratio of specific heats γ taken as 1.4. The ratio of the acoustic impedance for water and gas is

$$\frac{(\rho c)_{\text{water}}}{(\rho c)_{\text{gas}}} \approx 3.6 \times 10^3. \tag{3.1}$$

Owing to this large impedance mismatch, we expect almost total reflection when a weak shock wave, propagating in water, impacts the gas cavity.

In the computational domain we used 8 meshes in the r-direction and 16 meshes in the z-direction to define the gas bubble. A total of 80×160 meshes are used for the entire computational domain. Approximately 24 meshes from the bubble centre, the mesh size increases with a ratio of 1.05, making the size farther away from the bubble larger. This design of meshes uses less computational time than uniform meshes, while maintaining a good resolution near the gas cavity.

Figure 5 shows the Mach contour when a shock ($p/p_0 = 205$) impinges on a cavity ($R_0 = 0.01$ cm). The time interval between each successive plot is 0.1 μs. The shock front and rarefaction waves can be seen clearly in the water as well as in the gas. In figure 5(*a*), the shock front has just impacted the gas cavity. In figure 5(*b*), the shock propagates into the gas, and a rarefaction wave propagates away from the gas cavity after the shock interacts with the gas–water interface.

When the shock, propagating in the water, reaches the top wall of the bubble, it separates from the cavity (figure 5*c*) and continues to propagate away from it. There is no significant deformation of the bubble wall during this time because the shock is weak and the particle speed behind the shock front is much smaller than the shock speed.

The remaining plots in figure 5 show the convergence of the shock wave within the gas and the increase of Mach number in the water surrounding the gas driven by the pressure gradients near the cavity. Figure 5(*d*) shows that the location of convergence of the shock within the gas is close to the bottom of the cavity. Although the transmitted shock in the gas will converge, the resulting pressure increase in that region is not significant since the transmitted shock in the gas is very small owing to the impedance mismatch of gas and water.

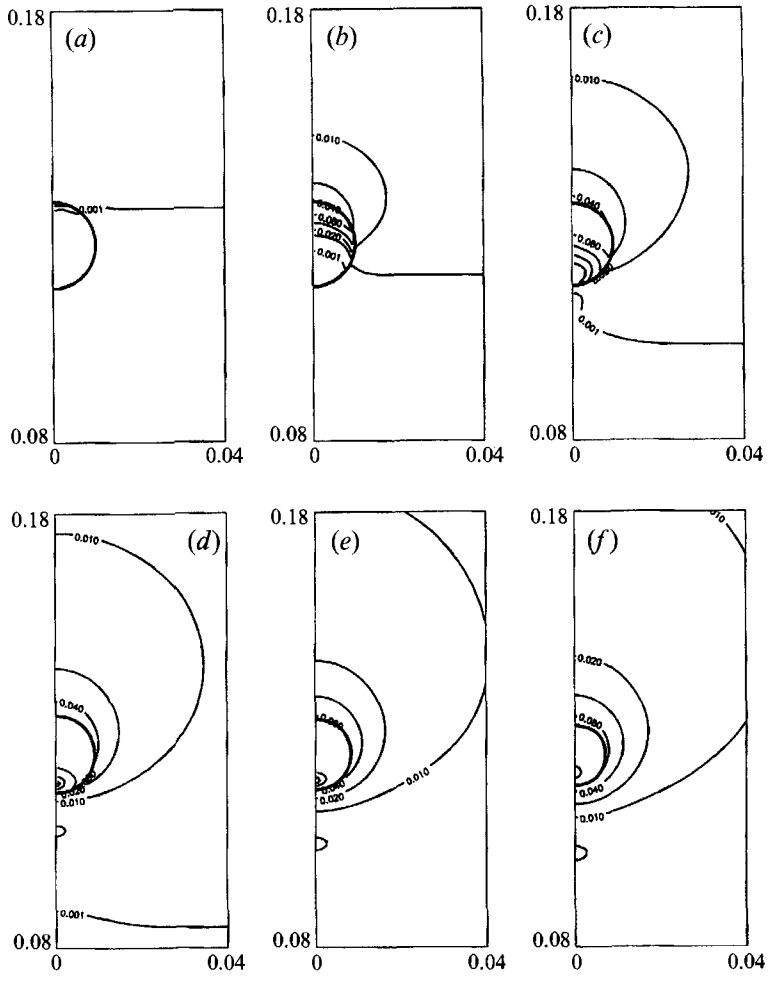

FIGURE 5. Mach contour of a gas cavity ($R_0 = 0.01$ cm) impacted by a weak shock ($p/p_0 = 205$). The time interval between each plot (*a–f*) is 0.1 μs.

In the one-dimensional, spherically symmetric models for bubble dynamics, the shock pressure is assumed to act instantaneously in the geometrical space. In reality, the shock propagates and encounters and passes the gas cavity from one side to the opposite side in a finite amount of time. This will produce non-spherical movement of the gas–water interface that cannot be represented in the one-dimensional model. However, for weak shocks, the interface motion is small during the time it takes for the shock front to pass over the cavity and therefore the non-spherical motion is not an important contributor to the subsequent cavity collapse.

Figure 6 shows the pressure field around the gas cavity for the same problem as above. The time interval between each plot is 0.15 μs. Figure 6(*a*) shows the pressure at time $t = 0$, the time at which the shock front just reaches the top of the gas cavity. In figure 6(*b*), the shock front has just passed the gas cavity, with the rarefaction wave spreading in water around the cavity. This creates a pressure gradient which drives the fluid towards the cavity. In figure 6(*c*,*d*), the pressure surrounding the cavity begins to further increase owing to the convergence of the water toward the gas cavity

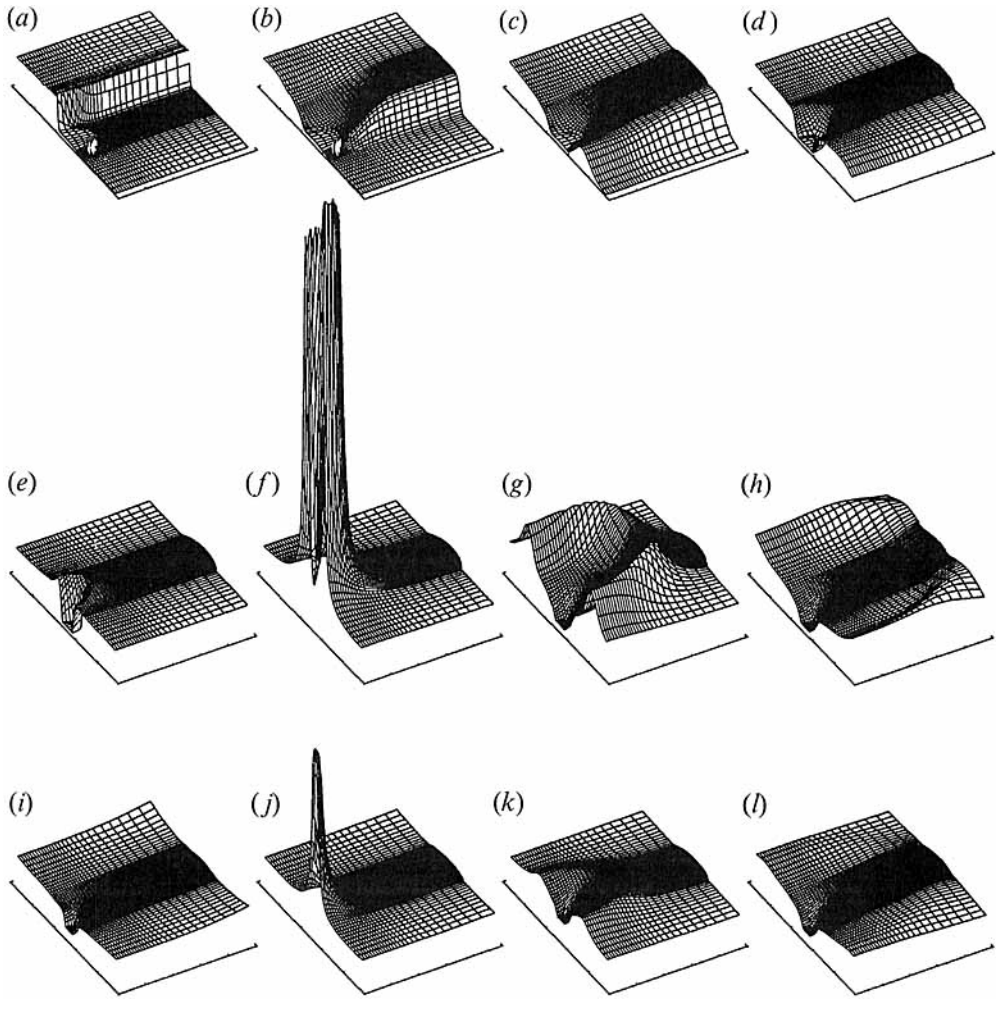

FIGURE 6. Pressure field of a gas cavity ($R_0 = 0.01$ cm) impacted by a weak shock ($p/p_0 = 205$). The time interval between each plot is 0.15 μs.

and the pressure gradient around the cavity is significantly larger than other regions far away from the cavity.

In figure 6(*e*), the liquid pressure surrounding the gas cavity is increased to a level higher than the shock strength, i.e. the pressure surrounding the gas cavity is larger than 20.5 MPa. At this stage, the volume of the gas cavity has still not significantly decreased, and the gas pressure remains much lower than that in the surrounding water. The large pressure gradients surrounding the cavity interface will rapidly drive the interface inward, and the fast convergent motion of the liquid particles surrounding the cavity carries a large inertia, which when resisted by the gas will create a large pressure increase. The high pressure gradient and the inertia of the convergent moving liquid cause a violent collapse of the gas cavity. The gas is compressed to a volume of about 0.042 % of the original volume, and the gas pressure reaches a value larger than 7 GPa at the cavity centre, owing to the rapid compression.

Next, the large pressure within the gas drives the liquid outward from the gas cavity. The gas cavity expands. In figure 6(*f*), the gas cavity is expanding, a pressure

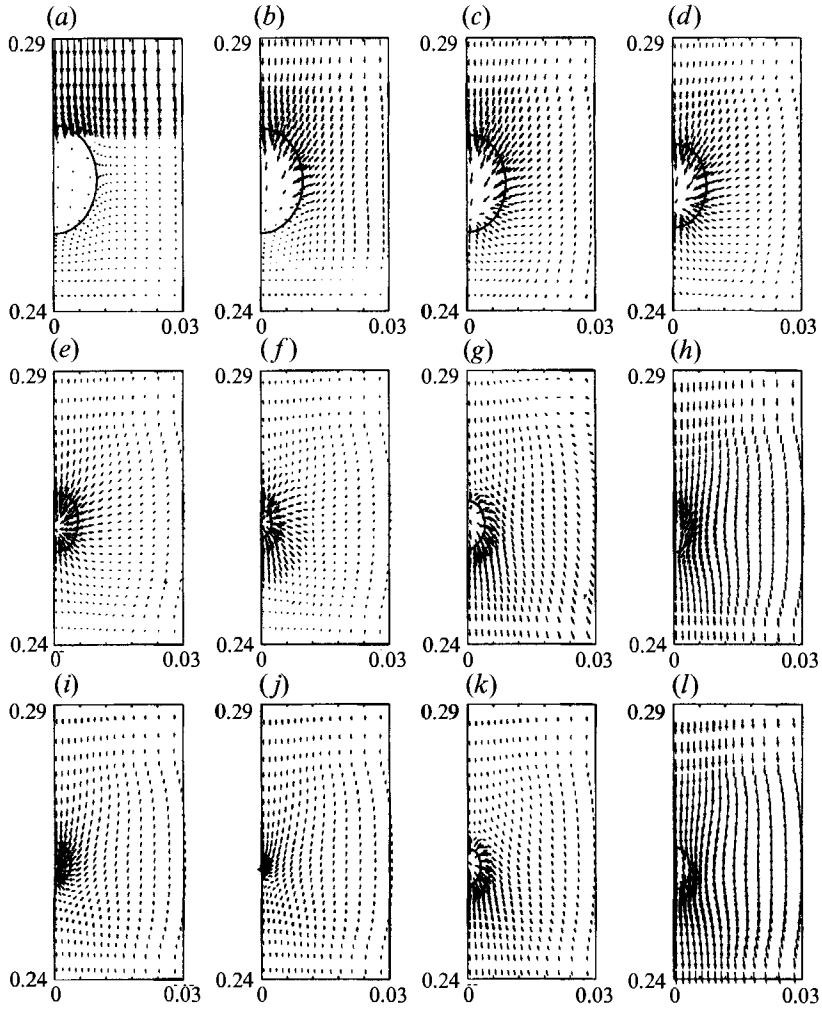

FIGURE 7. Velocity field of a gas cavity ($R_0 = 0.01$ cm) impacted by a weak shock ($p/p_0 = 205$). The time interval between each plot is 0.15 μs.

wave is propagating away from the gas cavity, and the gas pressure within the cavity is decreasing due to the expansion. Figure 6(*g*) shows the outward propagation of the pressure wave generated by the compressed gas. The cavity continues to expand owing to the inertia of the fluid particles, and the gas pressure drops even further.

Figure 6(*h*,*i*) shows that the pressure gradient surrounding the gas cavity again begins to drive the liquid toward the gas cavity. Figure 6(*j*) shows the second rapid compression of the gas. The gas pressure again reaches a level higher than in the surrounding liquid, creating a large pressure gradient to drive the liquid flow outward from the gas cavity. However the amplitude of the pressure is smaller than for the first collapse. Figure 6(*k*,*l*) shows the gas cavity expanding and the pressure wave propagating away from the gas cavity. The pressure within the gas cavity is again lower than in the surrounding liquid owing to cavity expansion, and the pressure gradient will drive the fluid to flow toward the gas cavity again, compressing the gas. This pattern of compression and expansion of the gas cavity will repeat with decreasing pressure amplitude, until the equilibrium state is reached.

Figure 7 shows the velocity vector fields for the same time sequence as figure 6. The amplitude of the velocity is normalized within each plot. Figure 7(*a*) is at the time when the shock front reaches the top of the gas cavity. The particles behind the shock front flow in the shock propagation direction with a constant speed of 13.5 m s^{-1}. In figure 7(*b*) the shock front has already passed the gas cavity, and the particles near the gas cavity are flowing toward the gas cavity driven by the pressure field. The velocity at the top of the gas cavity is higher than that at other locations. The bottom of the gas cavity has just begun to accelerate upward at this moment ($t = 0.15$ μs). The shock wave also propagates into the gas cavity. The particles, driven by the pressure gradient, move inward toward a point slightly below the centre of the cavity. In figure 7(*c,d*), the gas–water interface is further accelerated, moving inward, and the volume of the gas cavity continues to decrease. In figure 7(*e*), the gas–water interface is accelerated further by the pressure gradient. At this time, the cavity collapses violently.

Figure 7(*f*) shows the rapid expansion of the cavity after its violent collapse. The velocities at the gas–water interface have the highest amplitude and move the interface outward. Figure 7(*g*) shows the continued expansion of the gas cavity, with slower velocities along the gas-water interface. The downward migration of the gas cavity can be clearly seen in this plot. In figure 7(*h*), the fluid begins to flow inward, leading to the second compression of the gas cavity. At this moment, the velocity of the inward motion is not large compared with the first collapse. The downward migration of the cavity is much larger than the motion toward the gas cavity centre. In figure 7(*i, j*) the fluid is flowing inward toward the gas cavity, compressing the gas rapidly. The rapid compression of the gas will lead to a rapid increase of gas pressure as shown in figure 6, which will drive the gas-water interface outward. Figure 7(*k*) shows the expansion of the cavity and the outward motion of the gas-water interface. In figure 7(*l*), the speed of expansion is reduced, and the downward migration of the gas cavity again dominates the motion of the cavity and the surrounding fluid.

Figure 8 shows the computation mesh and the shape of the gas–water interface for the above problem. In the initial computation mesh, the cells surrounding the gas cavity are much finer than those within the gas cavity. This design of the mesh is due to the consideration that there will be a much larger pressure gradient in the liquid surrounding the gas cavity than within the gas cavity. When the cavity is compressed, the mesh size within the gas cavity will decrease dramatically. With the initial coarse mesh, the cells within the gas cavity will not become too small when the cavity collapses, therefore an acceptable computation time step can be maintained. The mesh in the liquid surrounding the gas–water interface is maintained to be much finer than other regions in the computation domain due to large pressure gradients near the interface. This is achieved by using the adaptive mesh generation techniques introduced in § 2.3.3.

The velocities and the pressure at the top and bottom of the gas–water interface are shown in figure 9 as function of time. The solid curve in figure 9(*a*) is the interface velocity at the cavity top. The dashed curve is the interface velocity at the cavity bottom. The dotted curve is the interface velocity predicted by the Gilmore model with rise time $\tau = 0.02$ μs.† When the shock hits the interface, the top of the interface

† The rise time τ for the step shock used in the Gilmore (1952) model is 0.02 μs for a cavity with initial radius of 0.01 cm. Since in the two-dimensional computations, the shock front is represented by about 6 cells, and spread in a range of about 0.003 cm, it will take about 0.02 μs for the shock strength to rise from p_0 to p. Similarly, for an initial cavity radius of 0.1 cm, the rise time is 0.2 μs. For a 1 cm cavity, the rise time is 2μs.

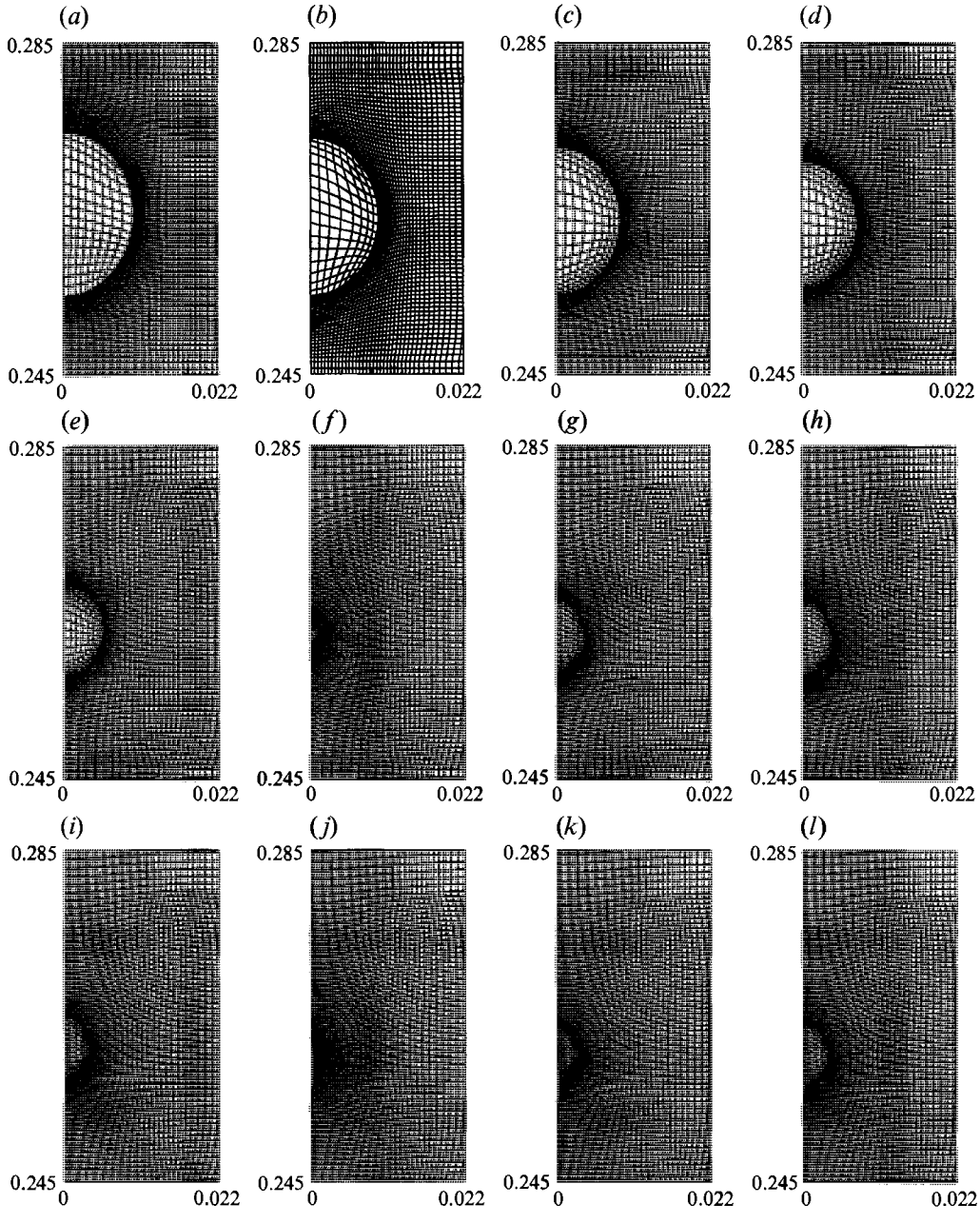

FIGURE 8. Computational mesh for a gas cavity ($R_0 = 0.01$ cm) impacted by a weak shock ($p/p_0 = 205$). The time interval between each plot is 0.15 μs.

is forced into the gas cavity with a velocity of approximately 25 m s^{-1}, about twice the velocity of the particles behind the shock front (a factor of 2 is what shock theory would predict for particles 'spalled' from a free surface). It will take about 0.02 μs for the shock to pass around the entire cavity; the motion of the cavity bottom is delayed by that amount of time. There is no jump of velocity at the bottom of the cavity.

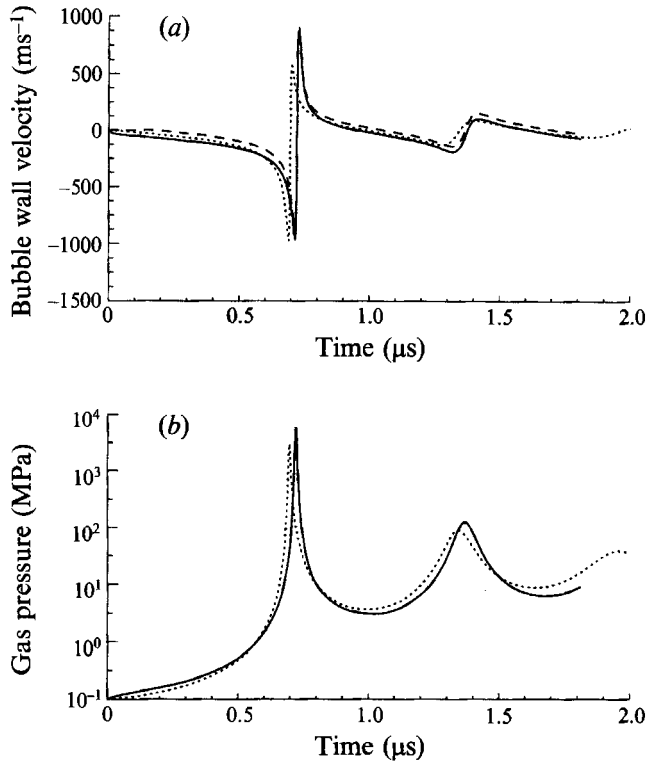

FIGURE 9. The velocity and gas pressure of a $R_0 = 0.01$ cm gas cavity subjected to a shock with $p/p_0 = 205$. (*a*) The cavity wall velocity: ——, velocity of cavity top; – – –, velocity of cavity bottom; . . . . . , cavity wall velocity predicted by Gilmore model. (*b*) Gas pressure: ——, gas pressure at the cavity top; . . . . . , gas pressure predicted by the Gilmore model.

The solid curve in figure 9(*b*) is the gas pressure at the top of the cavity. The dotted curve is the gas pressure predicted by the Gilmore model. The pressure field surrounding the cavity will drive the interface into the gas cavity, causing it to violently collapse at $t \approx 0.712$ μs, with the interface velocity −963 m s^{-1}.† Owing to the rapid compression of the gas in the cavity, the gas pressure at the top of the cavity will increase to nearly 6 GPa at the time of cavity collapse. This rapid increase of pressure within the gas will reverse the movement of the interface violently, causing the interface to move outward. Within 0.015 μs, the interface velocity will change to 884.9 m s^{-1} from −963 m s^{-1}. This rapid cavity expansion will cause the gas pressure to drop to a level lower than in the surrounding water. An inward motion of the interface begins at $t = 0.9$ μs. Another rapid compression occurs, and the cavity collapses again at $t = 1.37$ μs. The collapse velocity is about −200 m s^{-1} this time, and the collapse pressure of the gas at the cavity top is about 129 MPa. The second collapse of the cavity is much less violent than the first one, and the outward speed is much smaller. It takes about 0.09 μs for the interface velocity to change from −200 to 100 m s^{-1}. The computed results also show that the Gilmore model agrees very well with the two-dimensional results for the interface movement and the gas pressure in this particular case.

† The minus sign indicates that the interface is moving into the cavity. And a positive value indicates the interface is moving outward.

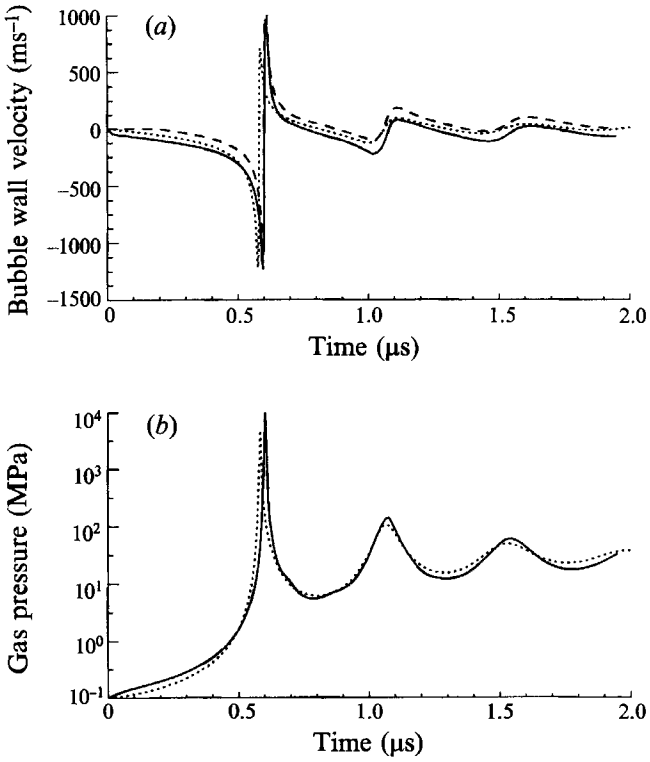

FIGURE 10. The velocity and gas pressure of a $R_0 = 0.01$ cm gas cavity subjected to a shock with $p/p_0 = 300$. (*a*): The cavity wall velocity: ——, velocity of cavity top; – – – , velocity of cavity bottom; . . . . . , cavity wall velocity predicted by Gilmore model. (*b*) Gas pressure: ——, gas pressure at the cavity top; . . . . . , gas pressure predicted by the Gilmore model.

When the shock strength is increased to $p/p_0 = 300$, the behaviour of the gas cavity and the pressure wave forms are quite similar to the case shown above but the collapse of the cavity is more violent. Figure 10 shows the velocity and gas pressure of a 0.01 cm gas cavity impacted by a shock with $p/p_0 = 300$. The interface velocity and gas pressure predicted by the Gilmore model are also plotted as a comparison. The collapse velocity for the top of the bubble wall is -1233 m s^{-1}, and the maximum expanding velocity at the top of the interface is 963 m s^{-1}. Owing to the increase of the shock strength, the cavity collapses sooner and more violently. The collapse time is 0.59 μs. The collapse pressure in the water at the top of the gas cavity is 7.31 GPa, and at the bottom it is 7.47 GPa. The collapse gas pressure at the top of the cavity is 10 GPa, at the centre it is 15 GPa, at the bottom it is 11.9 GPa.

The change of the initial cavity size will significantly change the collapse time. For a cavity with initial radius $R_0 = 0.1$ cm impacted by a shock with $p/p_0 = 205$, the collapse time is 7.02 μs. The velocity at the top and bottom of the interface and the gas pressure at these locations are shown in figure 11. The results computed with the Gilmore model are also presented in the same figure. At the time of collapse, the maximum interface speed (-1037 m s^{-1} at the top, and -1091 m s^{-1} at the bottom) is faster for the larger gas cavity. But the maximum expansion velocity (590 m s^{-1} at the top, and 696 m s^{-1} at the bottom) is smaller. The maximum gas pressures (7.8 GPa at the cavity centre, 5.1 GPa at the top, and 5.4 GPa at the bottom) are

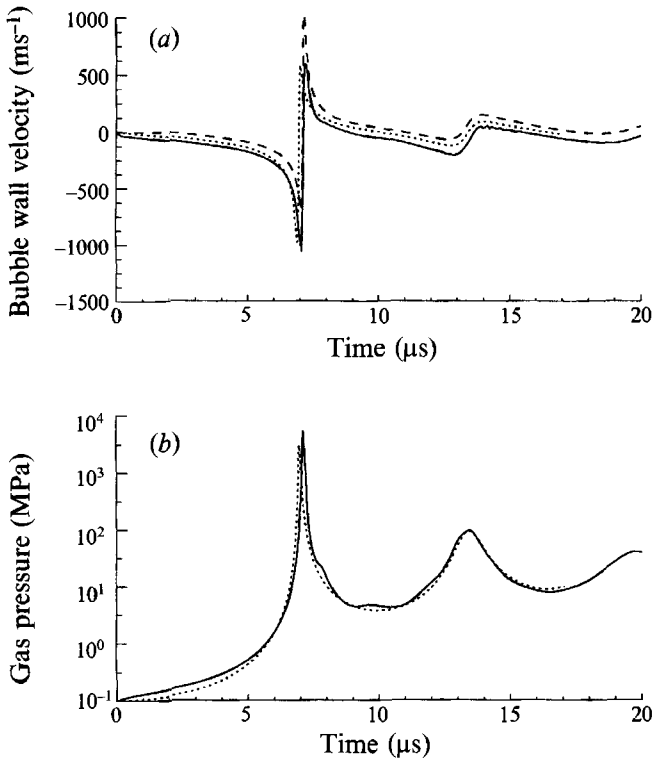

FIGURE 11. The velocity and gas pressure of a $R_0 = 0.1$ cm gas cavity subjected to a shock with $p/p_0 = 205$. (*a*) The cavity wall velocity: ——, velocity of cavity top; – – –, velocity of cavity bottom. . . . . , cavity wall velocity predicted by Gilmore model. (*b*) Gas pressure: ——, gas pressure at the cavity top; . . . . . , gas pressure predicted by the Gilmore model.

smaller for larger cavities as well. For a 1 cm cavity, the collapse time is 73.2 μs. The collapse pressure at the centre of the cavity is 4.6 GPa. The general behaviour is similar to that of the 0.01 cm gas cavity.

3.2. *Response to strong shock waves*

When a strong shock is applied, the nonlinearities of the flow are large, and the rarefaction spreads over a larger distance. Compared with the weak shock, the particle velocity behind the shock is also much larger for the strong shock, therefore a much larger momentum will impact the gas–water interface when the shock front hits the gas cavity. For a shock with $p/p_0 = 5280$, the particle speed behind the shock front is 255 m s^{-1}. For shock strength $p/p_0 = 10100$, it is 419 m s^{-1}. And for $p/p_0 = 2060$, the speed is 700 m s^{-1}.

The initial conditions for the gas bubble and surrounding water are the same as those in the weak shock problem. Eight meshes in the r-direction and 8 meshes in the z-direction are used for the gas. A total of 60 × 90 meshes are used in the whole computational domain.

Figure 12 shows the Mach contours for a shock ($p/p_0 = 5280$) impacting a gas cavity ($R_0 = 0.1$ cm). The time interval between each plot is 0.2 μs. At $t = 0$ (figure 12*a*), the shock just impacted the gas cavity, and the top of the gas cavity is forced into itself with a speed of about 500 m s^{-1}, approximately twice the particle speed behind the shock front. This speed is higher than the sound speed of gas, driving the

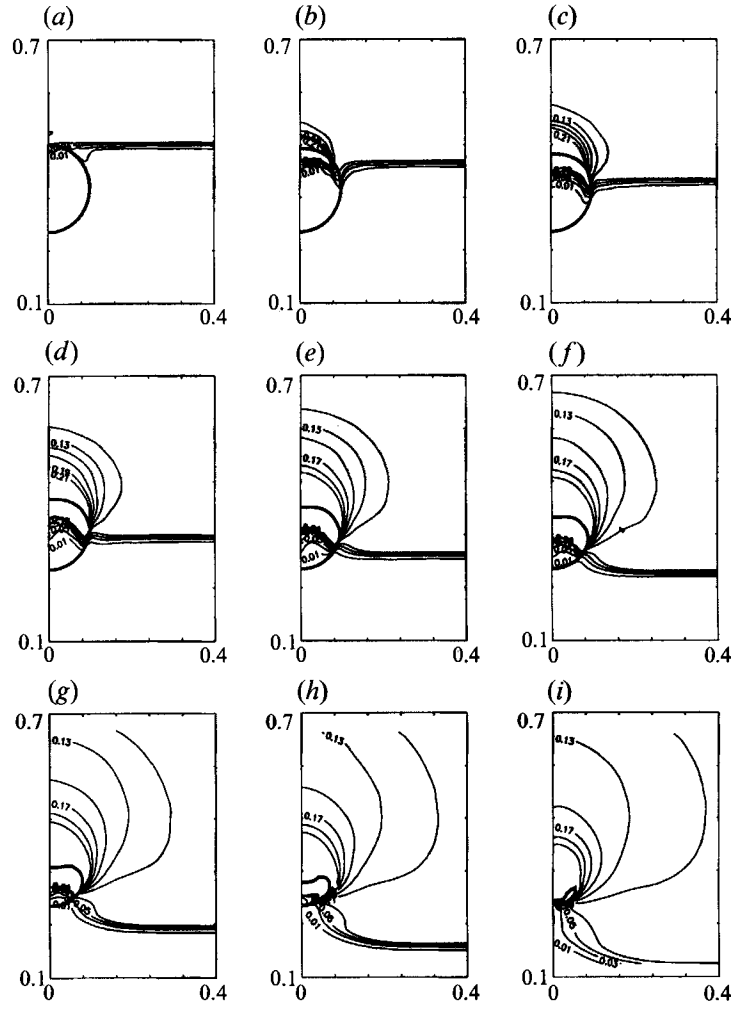

FIGURE 12. The Mach contours of a gas cavity ($R_0 = 0.1$ cm) collapsed by a shock with strength of $p/p_0 = 5280$. The time interval between each plot is 0.2 μs.

to form a shock propagating downward. Figure 12(*b*,*c*) shows the large rarefaction wave in water, and the shock propagation in the gas cavity. The interface is deformed rapidly as well. The non-symmetric movement of the interface is obvious with the bottom of the cavity remaining static. The shock propagation in the gas cavity will not converge to a point as in the weak shock situation. Figure 12(*d*–*f*) shows the spreading of the rarefaction wave as well as the shock propagation in the water and cavity. Even though the shock has not yet reached the bottom of the cavity so that it has not yet begin to move, the top of the cavity has already moved halfway across the centre of the cavity. Figure 12(*g*,*h*) shows the shock front within the gas reaching the bottom of the cavity: however the bottom of the cavity has not moved significantly. And the top of the cavity has already formed a jet, which will penetrate the bottom of the cavity at $t = 1.6$ μs (figure 12*i*).

Figure 13 shows the pressure contours of the above problem. At $t = 0$, the shock front reaches the top of the gas cavity (figure 13*a*). Figure 13(*b*,*c*) shows the large rarefaction of the shock wave. Figure 13(*d*) shows the top of the interface being forced

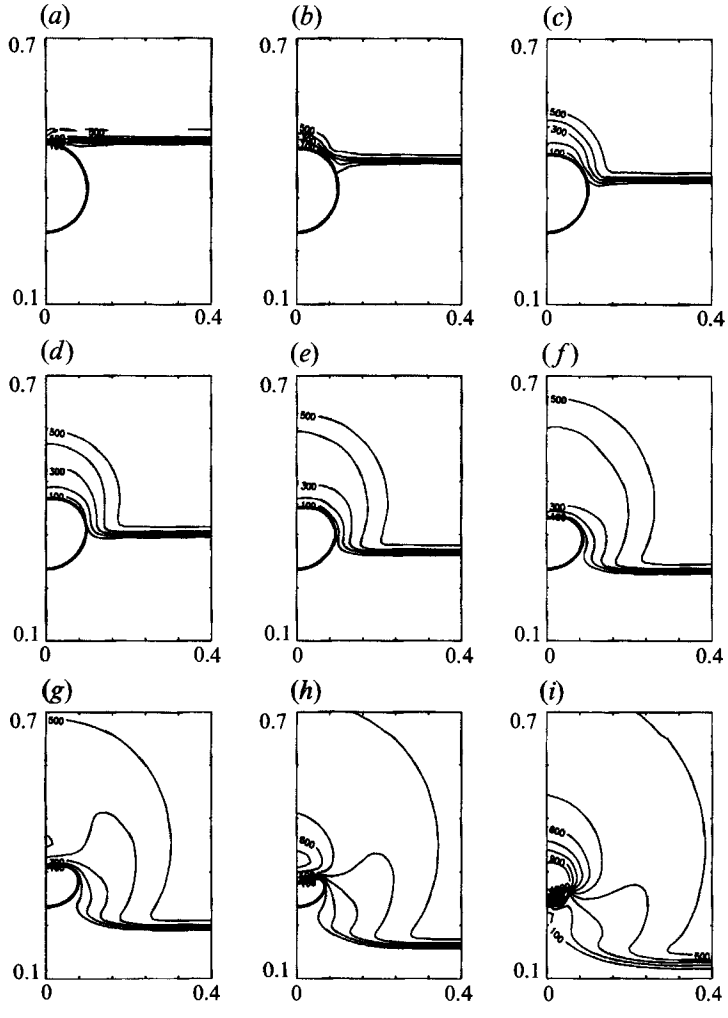

FIGURE 13. The pressure contours of a gas cavity collapsed by a shock with strength of $p/p_0 = 5280$. The time interval between each plot is 0.2 μs.

into the cavity, while the shock is just halfway across the cavity. Figure 13(*e*,*f*) shows the spreading of the rarefaction wave, and the top of the gas cavity is rapidly moving towards its opposite side. The pressure gradient in the water near the cavity top is even higher than at previous times.

The curvature of the pressure contours indicates that the pressure gradient is not convergent to a point within the gas cavity. Instead, the pressure gradient above the gas cavity will drive the fluid to flow to the location above the top of the deformed cavity which is approximately the centre of the cavity in its undeformed configuration. This motion of the fluid particles will cause stagnation above the top of the cavity and therefore a pressure increase is expected. Figure 13(*g*) ($t = 1.2$ μs) shows the increase of pressure above the cavity. This pressure build up continues as shown in figure 13(*h*,*i*), and a larger pressure gradient above the gas cavity further accelerates the motion of the cavity top. A jet with speed of 2200 m s^{-1} (at $t = 1.6$ μs) is about to penetrate the opposite side of the cavity.

The pressure on the top of the gas cavity can reach as high as 1 GPa before the

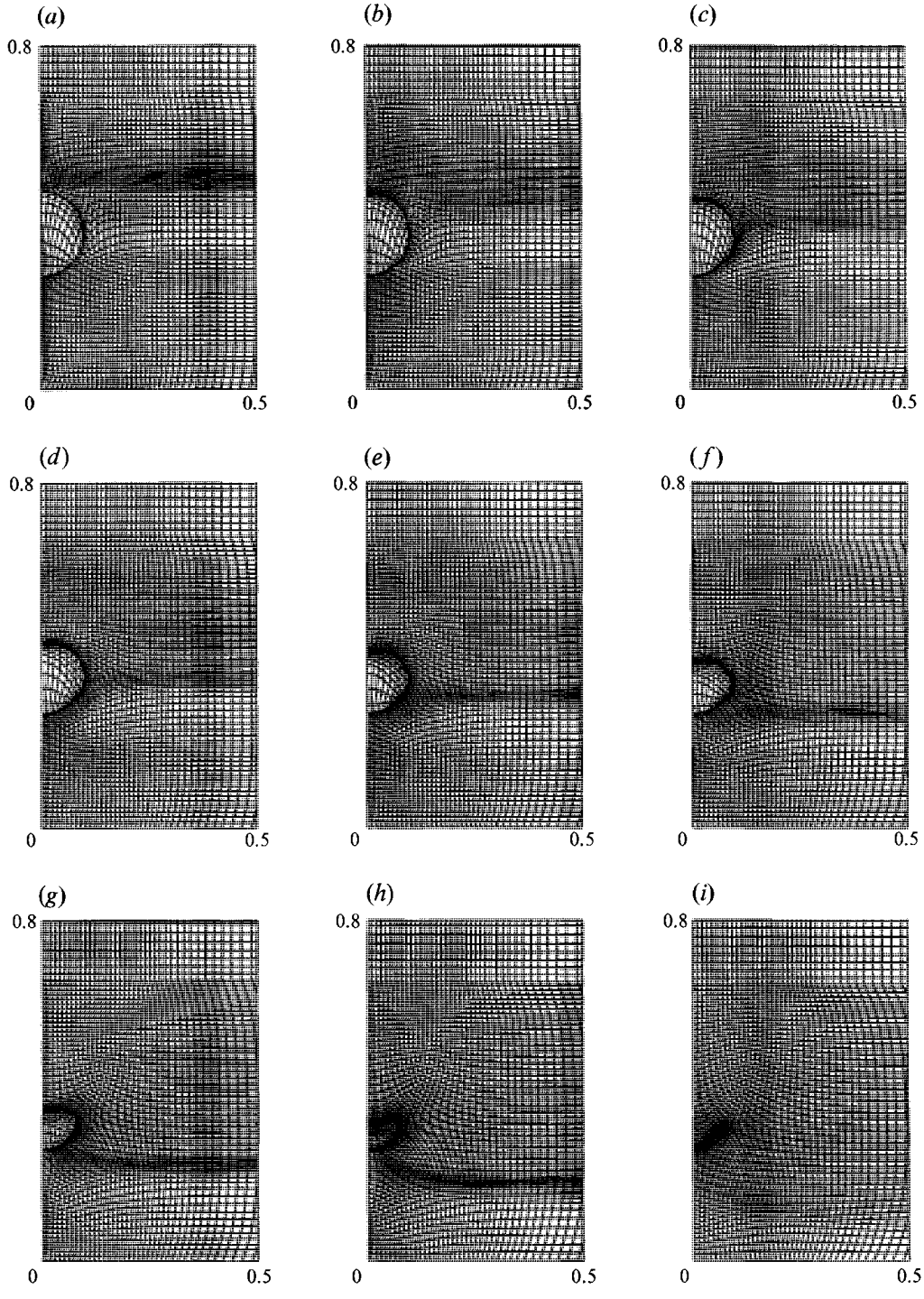

FIGURE 14. The computation mesh for a gas cavity with initial cavity size $R_0 = 0.1$ cm, and the shock strength $p/p_0 = 5280$. The time interval between each plot is 0.2 μs.

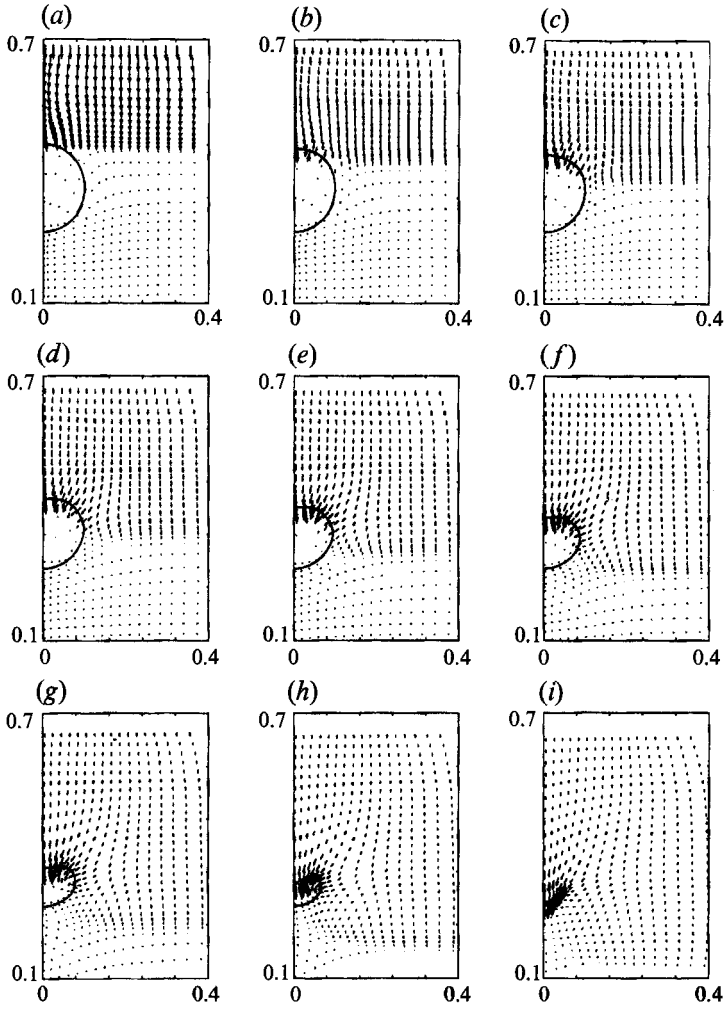

FIGURE 15. Velocity field surrounding a gas cavity ($R_0 = 0.1$ cm) impacted by a strong shock ($p/p_0 = 5280$). The time interval between each plot is 0.2 μs.

jet reaches the bottom of the gas cavity. Because the cavity volume variation is not large, the gas compression is small and the gas pressure does not increase much.

Figure 14 shows the computation mesh for this problem. Figure 14(*a*) is at the time when the shock just reaches the top of the gas cavity ($t = 0$). The time interval between each plot is 0.2 μs. The gas cavity collapses at 1.6 μ s (figure 14*i*). With the adaptive mesh generation techniques, the mesh automatically adapted to the pressure gradient. Here, at the shock front and the area around the gas cavity, the pressure gradients are higher. Therefore the meshes in these regions are finer. At $t = 1.6$ μs, we terminated the computations, since the meshes within the gas cavity are too small, and the time step became unacceptably small.

Figure 15 shows the velocity field surrounding the gas cavity. In figure 15(*a*), the fluid particles behind the shock front have the same velocity and direction. The particles in other regions remain static. Figure 15(*b*) shows the shock impacting the top of the cavity; the top of the interface is forced into the gas cavity with a speed equal to approximately twice the speed of the particles behind the shock front due

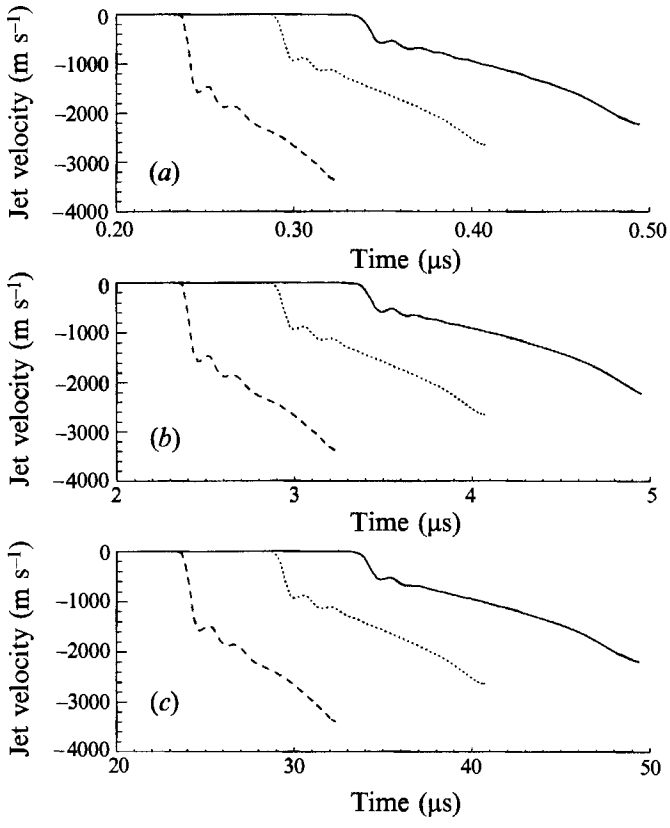

FIGURE 16. The velocities of the jet. The solid curves represent velocities with $p/p_0 = 5280$. The dotted curves represent velocities with $p/p_0 = 10110$. The dashed curves represent velocities with $p/p_0 = 20600$. (*a*) Initial cavity radius is 0.01 cm. (*b*) Initial cavity radius 0.1 cm. (*c*) Initial cavity radius 1 cm.

to the impedance mismatch between gas and water. As the rarefaction wave spreads away from the top of the gas cavity, the pressure gradients drive the particles to flow toward the gas cavity. Unlike the convergence movement as seen in the weak shock situation, the velocity component in the downward direction is always large. Figure 15(*d–f*) shows the upper part of the cavity interface moving rapidly downward, while the lower part of the cavity remains static. The asymmetric movement of the cavity continues and the jet speed will reach its highest value at $t = 1.6$ μs.

We also computed the cases with initial gas cavity sizes of $R_0 = 0.01, 0.1$, and 1 cm, and with the shock strengths of $p/p_0 = 5280$, 10110 and 20600. The general patterns of the gas cavity collapse, the rarefaction of the shock wave and the velocity profiles of the jet are similar. Figure 16 shows the velocities of the cavity top (the jet) with initial radius of 0.01 cm (*a*), 0.1 cm (*b*) and 1 cm (*c*). The larger the gas cavity, the longer the collapse time, but the collapse velocities are almost the same, independent of the initial cavity size. They are only a function of the applied shock strength.

4. Summary

The responses of gas cavities to both weak and strong shock waves were analysed. For a weak shock, the Gilmore model provides an accurate prediction of gas bubble response. The non-spherical movement of the interface is small, so the gas cavity

will collapse without jet formation. This collapse generates a large pressure in the gas cavity and the surrounding water by the rapid compression of the gas, radiating a pressure wave propagating away from the gas cavity. The gas cavity will expand after the collapse, and will collapse again with a weaker compression of the gas. This pattern of compression and expansion will continue until the gas cavity reaches an equilibrium state in the liquid. The larger the initial size of the gas cavity, the longer it will take to collapse. The collapse pressure of the gas cavity will slightly decrease as the initial gas cavity size increases.

For strong shocks, a jet will be created after the shock wave impacts the interface, and therefore the Gilmore model is not applicable. The jet will penetrate to the opposite side of the interface with a speed as high as 2000 m s^{-1}. The jet speed is almost independent of the initial gas cavity size, but depends on the applied shock strength. The gas within the cavity is not compressed seriously by the deformation of the cavity. Therefore, the gas pressure increase is small compared with the weak shock case. The stronger the applied shock, the higher the jet speed will be, and the sooner the gas cavity will collapse.

The general pattern of the rarefaction and transmission of shock waves of the a cavity impacted by weak or strong shocks agrees very well with the numerical results presented by Grove & Menikoff (1990). They investigated the early stages of shock–interface interaction without studying the details of the collapse of the gas cavity. The shape of the collapsed gas cavity also qualitatively agrees with the experimental observations of Dear & Field (1987, 1988) and Bourne & Field (1990).

REFERENCES

BAILEY, M. R., DALECKI, D., CHILD, S. Z., RAEMAN, C. H., BLACKSTOCK, D. T. & CARSTENSEN, E. L. 1995 Bioeffect of positive and negative acoustic pressure *in vivo*. Submitted for publication.

BENSON, D. J. 1991 A new two-dimensional flux-limited shock viscosity for impact calculation. *Comput. Meth. Appl. Mech. Engng* **93**, 39–95.

BLAKE, J. R. & GIBSON, D. C. 1987 Cavitation bubbles near boundaries. *Ann. Rev. Fluid Mech.* **19**, 99–123.

BOURNE, N. & FIELD, J. 1990 Collapsing cavities in reactive and non-reactive media. In *19th International Congress on High-Speed Photography and Photonics*, vol. SPIE 1358, pp. 1046–1056.

BRACKBILL, J. U. & SALTZMAN, J. S. 1982 Adaptive zoning for singular problems in two dimensions. *J. Comput. Phys.* **46**, 342–368.

CARSTENSEN, E. L., CAMPBELL, D. S., HOFFMAN, D., CHILD, S. Z. & AYME-BELLEGARDA, E. J. 1990 Killing of drosophila larvae by the fields of an electrohydraulic lithotripter . *Ultrasound Med. Biol.* **16**, 687–698.

CRUM, L. A. 1988 Cavitation microjets as a contributory mechanism for renal calculi disintegration in ESWL. *J. Urology* **140**, 1587–1590.

DEAR, J. P. & FIELD, J. E. 1987 Applications of the two-dimensional gel techniques to erosion problems. In *Proc. 7th Intl Conf. on Erosion by Liquid and Solid Impact*, pp. 4.1–4.11.

DEAR, J. P. & FIELD, J. E. 1988 A study of the collapse of arrays of cavities. *J. Fluid Mech.* **190**, 409–425.

DELIUS, M., ENDERS, G., HEINE, G., STARK, J., REMBERGER, K. & BRENDEL, W. 1987 Biological effects of shock waves: Lung hemorrhage by shock waves in dogs - Pressure dependence. *Ultrasound Med. Biol.* **13**, 61–67.

DELIUS, M., JORDAN, M., EIZENHOEFER, H., MARLINGHAUS, E., HEINE, G., LIEBICH, H. G. & BRENDEL, W. 1988 Biological effects of shock waves: Kidney hemorrhage by shock waves in dogs - Administration rate dependence. *Ultrasound Med. Biol.* **14**, 689–694.

DEMUTH, R. B., MARGOLIN, L. G., NICHOLS, B. D., ADAMS, T. F. & SMITH, B. W. 1985 SHALE: A computer program for solid dynamics. *Tech. Rep.* LA-10236. Los Alamos National Laboratory.

DING, Z. & GRACEWSKI, S. 1994 Response of constrained and unconstrained bubbles to lithotripter shock wave pulses. *J. Acoust. Soc. Am.* **96**, 3636–3644.

DWYER, H. A., KEE, R. J. & SANDERS, B. R. 1980 Adaptive grid method for problems in fluid mechanics and heat transfer. *AIAA J.* **18**, 1205–1212.

EVANS, M. W., HARLOW, F. H. & MEIXNER, B. D. 1962 Interaction of shock or rarefaction with a bubble. *Phys. Fluids* **5**, 651–656.

FLYNN, H. G. 1964 Physics of acoustic cavitation in liquids. In *Physical Acoustics* (ed. W. P. Mason), vol. 1, Part B, pp. 58–172. Academic.

GILMORE, F. R. 1952 The growth or collapse of a spherical bubble in a viscous compressible liquid. *Rep.* 26–4, pp. 1–40. California Institute of Technology, Pasadena, CA.

GRACEWSKI, S. M., DAHAKE, G., DING, Z., BURNS, S. J. & EVERBACH, E. C. 1993 Internal stress wave measurements in solid subjected to lithotripter pulses. *J. Acoust. Soc. Am.* **94**, 652–661.

GROVE, J. W. & MENIKOFF, R. 1990 Anomalous reflection of a shock wave at a fluid interface. *J. Fluid Mech.* **219**, 313–336.

HANSSON, I. & MORCH, K. A. 1980 The dynamics of cavity clusters in ultrasonic (vibratory) cavitation erosion. *J. Appl. Phys.* **51**, 4651–4658.

HAAS, J. F. & STURTEVANT, B. 1987 Interaction of weak shock waves with cylindrical and spherical gas inhomogeneities. *J. Fluid Mech.* **181**, 41–76.

HIRT, C. W., AMSDEN, A. A. & COOK, J. L. 1974 An arbitrary Lagrangian-Eulerian computing method for all flow speeds. *J. Comput. Phys.* **14**, 227–253.

JORDAN, S. A. & SPAULDING, M. L. 1993 A fast algorithm for grid generation. *J. Comput. Phys.* **104**, 118–128.

KORNFELD, M. & SUVOROV, L. 1944 On the destructive action of cavitation. *J. Appl. Phys.* **15**, 495–506.

LANDSHOFF, R. 1955 A numerical method for treating fluid flow in the presence of shocks. *Tech. Rep.* LA-1930. Los Alamos Scientific Lab.

LEER, B. V. 1977 Towards the ultimate conservative difference scheme. IV. A new approach to numerical conservation. *J. Comput. Phys.* **23**, 276–299.

LEER, B. V. 1979 Towards the ultimate conservative difference scheme. V. A second-order sequel to Godunov's method. *J. Comput. Phys.* **32**, 101–136.

MADAR, C. L. 1965 Initiation of detonation by the interaction of shocks with density discontinuities. *Phys. Fluids* **8**, 1811–1816.

MARGOLIN, L. G. 1988 A centered artificial viscosity for cells with large aspect ratio. *Tech. Rep.* UCRL-53882. Lawrence Livermore National Laboratory.

MATSUNO, K. & DWYER, H. A. 1988 Adaptive methods for elliptic grid generation. *J. Comput. Phys.* **77**, 40–52.

NEUMANN, J. V. & RICHTMYER, R. D. 1950 A method for the numerical calculation of hydrodynamic shocks. *J. Appl. Phys.* **21**, 232–237.

PHILIPP, A., DELIUS, M., SCHEFFCZYK, C., VOGEL, A. & LAUTERBORN, W. 1993 Interaction of lithotripter-generated shock waves with air bubbles. *J. Acoust. Soc. Am.* **93**, 2496–2509.

PICONE, J. M. & BORIS, J. P. 1988 Vorticity generated by shock propagation through bubbles in gas. *J. Fluid Mech.* **189**, 23–51.

PLESSET, M. S. & PROSPERETTI, A. 1977 Bubble dynamics and cavitation. *Ann. Rev. Fluid Mech.* **9**, 145.

PROSPERETTI, A. 1982 Bubble dynamics: a review and some recent results. *Appl. Sci. Res.* **38**, 145–164.

QUIRK, J. J. & KARNI, S. 1994 On the dynamics of a shock-bubble interaction. *NASA CR*-194978; *ICASE Rep.* pp. 94–75.

RAYLEIGH, LORD 1917 On the pressure developed in a liquid during the collapse of a spherical cavity. *Phil. Mag.* **34**, 94–98.

SASS, W., BRAUNLICH, M., DREYER, H., MATURA, E., FOLBERTH, W., PRIESMEYER, H. SEIFERT, J. 1991 The mechanisms of stone disintegration by shock waves. *Ultrasound Med. Biol.* **17**, 239–243.

SATO, K., TOMITA, Y. & SHIMA, A. 1994 Numerical analysis of a gas bubble near a rigid boundary in an oscillatory pressure field. *J. Acoust. Soc. Am.* **95**, 2416–2424

SCHWENDEMAN, S. D. 1986 Numerical shock propagation in non-uniform media. *J. Fluid Mech.* **188**, 383–410.

STEINBERG, D. J. 1987 Spherical explosions and the equation of state of water. *Tech. Rep.* UCID-20974. Lawrence Livermore National Laboratory.

STEINBERG, D. J. 1993 A brief review on cavitation bubble collapse near a rigid boundary. *J. Stone Disease* **5(1)**, 49–59.

THOMPSON, J. F., WARSI, Z. U. A. & MASTIN, C. W. 1985 *Numerical Grid Generation - Foundations and Applications.* North-Holland.

THOMPSON, P. A. 1988 *Compressible-Fluid Dynamics.* Rensselaer Polytechnic Institute, New York.

TIPTON, R. E., STEINBERG, D. J. & TOMITA, Y. 1992 Bubble expansion and collapse near a rigid wall. *JSME Intl J.* II **35(1)**, 67–75.

TRILLING, L. 1952 The collapse and rebound of a gas bubble. *J. Appl. Phys.* **23**, 14–17.

VAKIL, N. & EVERBACH, E. C. 1991 Gas in gallstones: quantitative determinations and possible effects on fragmentation by shock waves. *Gastroenterology* **101**, 1628–1634.

VOGEL, A., LAUTERBORN, W. & TIMM, R. 1989 Optical and acoustic investigations of the dynamics of laser-produced cavitating bubbles near a solid boundary. *J. Fluid Mech.* **206**, 299–338.

WILKINS, M. L. 1964 Calculation of elastic-plastic flow. *Meth. Comput. Phys.* **3**, 211–263.

WILKINS, M. L. 1980 Use of artificial viscosity in multidimensional fluid dynamics. *J. Comput. Phys.* **36**, 281–303.

WINSLOW, A. M. 1963 Equipotential zoning of two-dimensional meshes. *Tech. Rep.* UCRL-7312. Lawrence Livermore Radiation Laboratory.

ZHANG, S., DUNCAN, J. H. & CHAHINE, G. L. 1993 The final stage of the collapse of a cavitation bubble near a rigid wall. *J. Fluid Mech* **257**, 147-181.